UC Santa Barbara
UC Santa Barbara Previously Published Works

Title

Fidelity and variability in the interlayer electronic structure of the kagome superconductor CsV3Sb5

Permalink

https://escholarship.org/uc/item/5vk8g3gj

Journal

Physical Review Materials, 8(5)

ISSN

2475-9953

Authors

Watkins, Aurland K

Johrendt, Dirk

Vlcek, Vojtech

et al.

Publication Date

2024-05-20

DOI

10.1103/PhysRevMaterials.8.054204

Peer reviewed

Fidelity and variability in the interlayer electronic structure of the kagome superconductor CsV_3Sb_5

Aurland K. Watkins [1,*] Dirk Johrendt [2] Vojtech Vlcek [1,3] Stephen D. Wilson [1] and Ram Seshadri [1,3]

[1]*Materials Department, University of California, Santa Barbara, California 93106, USA*
[2]*Department Chemie, Ludwig-Maximilians-Universität München, 81377 Munich, Germany*
[3]*Department of Chemistry and Biochemistry, University of California, Santa Barbara, California 93106, USA*

The AV_3Sb_5 (A = K, Rb, Cs) kagome materials host an interplay of emergent phenomena including superconductivity, charge density wave states, and nontrivial electronic structure topology. The band structures of these materials exhibit a rich variety of features like Dirac crossings, saddle points associated with van Hove singularities, and flat bands prompting significant investigations into the in-plane electronic behavior. However, recent findings including the charge density wave ordering and effects due to pressure or chemical doping point to the importance of understanding interactions between kagome layers. Probing this c-axis electronic structure via experimental methods remains challenging due to limitations of the crystals and, therefore, rigorous computational approaches are necessary to study the interlayer interactions. Here we use first-principles approaches to study the electronic structure of CsV_3Sb_5 with emphasis on the k_z dispersion. We find that the inclusion of nonlocal and dynamical many-body correlation has a substantial impact on the interlayer band structure. We present band behavior that additionally supports the integration of symmetry in accurately plotting electronic structures and influences further analysis like the calculation of topological invariants.

I. INTRODUCTION

First-principles electronic structure calculations are critical for the identification and characterization of topological materials given the limited and complex experimental tools designed to confirm nontrivial electronic structure topology [1,2]. While bulk band structure features like band crossings or flat bands can point to nontrivial topology, confirmation requires additional techniques. There are three common computational or theoretical methods relying on the bulk band structure to classify topological materials: (1) adiabatically evolving the Hamiltonian to match the band structure of a material with known topology, (2) computing the surface electronic structure to directly detect topological surface states, and (3) calculating a topological invariant. This final method employs the underlying symmetries and features of the bulk band structure to produce an index describing the topology [3].

A $\mathbb{Z}_2$ invariant (ν) is used to distinguish between trivial ($\nu = 0$) and nontrivial ($\nu = 1$) time-reversal invariant systems with a bulk electronic gap by specifying whether topological surface states are expected to reside in this gap [4–6]. For systems that additionally possess inversion symmetry, Fu and Kane developed a protocol for calculating $\mathbb{Z}_2$ invariants that relies on the parity (inversion) of the Bloch wave functions defined at specific k points that are invariant under time-reversal symmetry. In a 3D Brillouin zone, there are eight of these k points known as time-reversal invariant momenta (TRIM) points. In the Fu-Kane protocol, the product of band parities across all bands below the gap is calculated at individual TRIM points. Subsequently, a product across all the TRIM point products is taken and the $\mathbb{Z}_2$ invariant is calculated [7].

While this method was originally developed for insulators or materials with band gaps, this type of $\mathbb{Z}_2$ analysis does not depend on band filling and, therefore, can be applied to metallic systems with partial band occupancy [8–10]. However, to extend this calculation to metals, the band structure must have a continuous gap throughout the Brillouin zone (BZ) located near the Fermi energy (E_F). This requirement ensures that the parity products at each of the TRIM points consistently include the same bands. This method was previously applied to metals featuring kagome nets to support their nontrivial $\mathbb{Z}_2$ classification [11,12].

The kagome net of corner-sharing triangles (Fig. 1) has drawn significant interest as a platform for a variety of instabilities and emergent phenomena like spin liquid states, superconductivity, charge density waves, and topological surface states [13–15]. Recently, materials within the AV_3Sb_5 (A = K, Rb, Cs) kagome family were categorized as $\mathbb{Z}_2$ topological metals following the Fu-Kane method [11,12]. The presence of two continuous gaps throughout the BZ near E_F allowed for the calculation of multiple $\mathbb{Z}_2$ invariants, both of which indicated nontrivial topology suggesting that CsV_3Sb_5 exhibits topological surface states analogous to a topological insulator. This original $\mathbb{Z}_2$ analysis relied on a band structure that was obtained via a structural relaxation with the PBE (Perdew-Burke-Ernzerhof) functional [16] and D3 correction with the addition of spin-orbit coupling (SOC) in the self-consistent calculation. The D3 correction is an empirical van der Waals total energy correction that was identified as a necessary parameter to more closely match experimental lattice
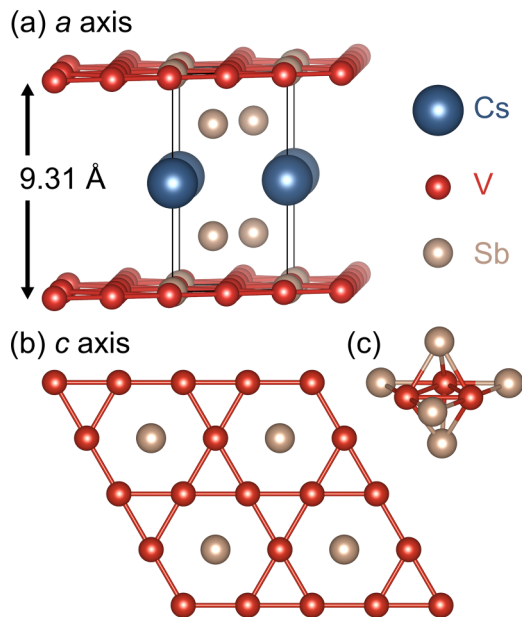
*aurland@ucsb.edu

FIG. 1. Crystal structure depictions of CsV_3Sb_5. (a) Quasi-2-dimensional structure highlighting separation between kagome sheets. (b) and (c) Coordination environment within and adjacent to kagome layers.

parameters (specifically along the *c* axis) during relaxation [17,18].

Here, we present electronic structure analysis of CsV_3Sb_5, with special consideration of anisotropic nonlocal correlation along the k_z or inter-kagome-plane direction. Within the framework of density functional theory (DFT), we find that including certain computational parameters during a structural relaxation gives rise to a symmetry-allowed band crossing previously not identified between Γ and A as highlighted in Fig. 2. This crossing is also observed when the calculations are performed on the experimental structure without relaxation. However, higher-level calculations on the experimental structure show gapped instead of crossed bands due to shifts in the positions of the bands. As the level of computational
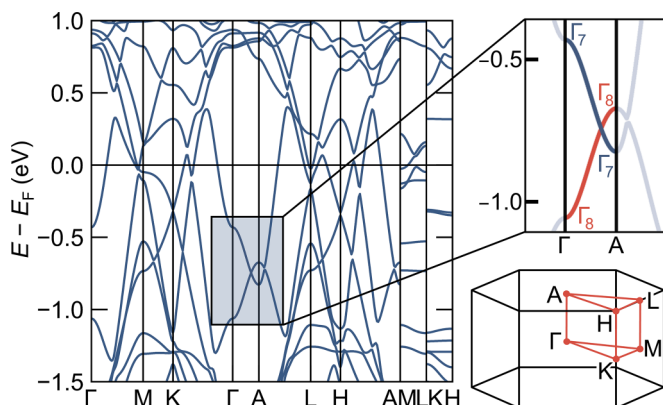

FIG. 2. PBE+SOC+D3 electronic structure of CsV_3Sb_5 along high-symmetry *k*-point path. A previously unidentified crossing along Γ-*A* representing the k_z-band dispersion is confirmed by irrep analysis.

theory increases, these energy shifts become more pronounced. Ultimately, this study suggests that it is critical to include nonlocal and dynamical many-body correlation through the application of the *GW* approximation to obtain accurate interlayer band behavior. The resulting electronic structure shows significant shifts of the bands that results in the almost degeneracy of a V band and an out-of-plane Sb band. This study of the seemingly minor region of the band structure additionally impacts the calculation of $\mathbb{Z}_2$ invariants in this material and points to a larger issue of correct band identification or tracking when plotting band structures.

II. METHODS

First-principles calculations were performed using the Vienna *ab initio* Simulation Package (VASP) version 5.4.4. Pseudopotentials following the projector-augmented wave method were selected with the following valence configurations: Cs ($5s^2 5p^6 6s^1$), V ($3s^2 3p^6 4s^2 3d^3$), Sb ($5s^2 5p^3$). An $11 \times 11 \times 5$ Γ-centered *k*-point mesh was automatically generated by VASP and the plane-wave energy cutoff was set to 500 eV. Geometric optimization or relaxation of the experimental structure (ICSD 31841) was performed with all listed parameters (for example, the structure for the PBE+SOC results came from a relaxation using PBE and SOC) [19]. During optimization, the first-order Methfessel-Paxton smearing scheme was employed with a smearing width of 0.2 eV and all degrees of freedom (atomic positions and cell shape/volume) were allowed to relax until forces were converged within 10^{-7} eV/Å [20]. Calculations based on the experimental structure were also performed and are referred to as "unrelaxed" calculations. The static self-consistent and non-self-consistent density of states (DOS) calculations used tetrahedral smearing with Blöchl corrections [21]. All nonhybrid DFT calculations had an energy convergence better than 10^{-8} eV. A *k*-point path for the band structure was generated using the AFLOW online tool and the density of the path was set to 50 *k* points per path segment (for example between Γ and *A*) to ensure high resolution of band features in the final plot [22]. Band structures were plotted using the sumo package [23]. Irreducible representations were obtained using the Irvsp program that interfaces with VASP outputs [24].

Meta-GGA (generalized gradient approximation) and hybrid functional band structures were calculated using the VASP-recommended protocol for these types of functionals. First, a ground state calculation was performed to obtain converged wave functions (for hybrid functionals, it is sufficient to use PBE for this step for faster convergence). This output served as the starting point for a self-consistent band calculation using a regular *k*-point mesh with an appended zero-weighted *k*-point path for the band structure. This protocol differs from standard non-self-consistent-field band calculations that require only the precoverged charge density (CHGCAR file) with a *k*-point path. However, both hybrid and meta-GGA functionals require a regular *k*-point mesh and, therefore, require this alternative band calculation procedure. The *k*-point file was generated using the hybrid option within the sumo package [23]. The energy convergence for the hybrid functional calculations was loosened to 10^{-6} eV.

GW calculations implemented in VASP were performed on the experimental (unrelaxed) structure and employed the PBE electronic structure as a starting point. Both single-shot G_0W_0 and partially self-consistent eigenvalue GW_0 (ev GW_0) calculations were performed. *GW* potentials were selected based on the VASP recommendations with the following valence configurations: Cs $(5s^25p^66s^1)$, V $(3s^23p^64s^23d^3)$, Sb $(4d^{10}5s^25p^3)$. The total number of bands was set to 4000 and the number of frequency points was set to 100. Given the high computational cost of *GW* calculations, a smaller $4 \times 4 \times 2$ *k*-point grid was used. This setup yields quasiparticle energies converged to within 50 meV. For the GW_0 calculation, seven steps were necessary for convergence; however, all results detailed in this study were taken after ten steps. Since the orbitals are not updated in the ev GW_0 self-consistency scheme, the interpolation of bands between Γ and A in the *GW* output should match that seen in standard DFT even as the eigenvalues are updated. To visualize the resulting band behavior, eigenvalues were matched to the ordering of states in DFT outputs. The interpolation of bands between Γ and A was preserved from the unrelaxed PBE band structure, yet it was scaled such that the end-point energies (at Γ and A) correspond to the updated eigenvalues from the *GW* calculations. Further details are provided in Appendix B.

III. RESULTS

A. General features of the band structure

The electronic structure of CsV_3Sb_5 hosts a variety of features associated with unique physical phenomena. Many computational efforts have focused on the Dirac crossings [25] and van Hove singularities [26] characteristic of the kagome electronic structure. Specifically, there is significant interest in the near-Fermi-level saddle points in the band structure that correspond to van Hove singularities or divergences in the density of states. Due to the high DOS, interactions can become pronounced when a saddle point becomes populated and can nest across the Fermi surface. In CsV_3Sb_5, multiple saddle points residing at the *M* point give rise to competing instabilities depending on band filling [26,27].

Yet, while the intralayer interactions draw focus, the interlayer electronic behavior is understudied [28]. Among kagome materials, the 135 family is highly two-dimensional as seen in the stacking of the kagome layers (Fig. 1). While these materials are not considered traditional 2D materials given the presence of *A*-site ions between the layers, previous electronic structure work concluded that van der Waals interactions were necessary to reproduce the experimental *c*-axis lattice parameter during structural relaxation. These interactions are most relevant along the interlayer or k_z direction represented along the Γ-*A* and *K-H* paths within the Brillouin zone. The near-Fermi-level bands along these paths are dominated by Sb p_z orbitals unlike the V character bands found elsewhere in the BZ [29].

B. Band crossing along Γ-*A*

When comparing published band structures for this material, there is a large degree of variability with respect to the band behavior between Γ and A, specifically around 0.75 eV

below the Fermi energy. These band structures can be categorized into three main groups depending on the interaction of the two bands in this energy range: (1) fully gapped bands [27,30,31], (2) seemingly touching bands with a minor gap [12,32], and (3) fully crossed bands with crossings between Γ and A and between A and L [33,34]. We similarly obtain these variations of electronic structures depending on the parameters included in the calculation and the methods employed for plotting. To understand the nature of and potentially validate these crossings, the symmetry or the irreducible representations (irreps) of the bands at specific *k* points need to be analyzed. When bands possess the same symmetry or irrep, the associated electronic states mix or hybridize and form a gap. Only when bands have different irreps can a symmetry-allowed crossing occur [35].

Irreps additionally change with the inclusion of SOC since a spinor representation (as opposed to a vector representation) is required to capture the spin symmetry. Within the Brillouin zone of CsV_3Sb_5, most of the paths connecting *k* points have C_{2v} symmetry which has only one spinor irrep. Since bands in these regions can only have this one irrep, all bands will be gapped from each other (i.e., no symmetry-dictated band crossings). However, the paths along Γ-*A* and *K-H* have C_{6v} symmetry with multiple spinor irreps allowing for crossings. Therefore, when SOC is included, these are the only two regions of the Brillouin zone that matter for identifying a continuous gap. This means that even though Γ and A only represent two of the eight TRIM points necessary for calculating a $\mathbb{Z}_2$ topological invariant, these *k* points are critical for determining whether this calculation can be performed in the first place (a continuous gap is a prerequisite for a Fu-Kane type $\mathbb{Z}_2$ calculation).

It is important to note that "symmetry-allowed crossing" does not refer to symmetry-*enforced* crossings arising from nonsymmorphic symmetries. While the crossings of interest are dictated or "enforced" by the differing symmetries of the bands, we avoid this terminology since it already has a specific definition within topological band theory [36,37].

When band symmetry is included in the previously optimized calculations for CsV_3Sb_5 (relaxed with PBE+D3 followed by PBE+D3+SOC ground state calculation in [12]), multiple band crossings are observed along Γ-*A* and *K-H*. Since the band behavior between Γ and A conflict with previous reports, those crossings are the focus of this study. Based on symmetry considerations, the two bands around 0.75 eV below the Fermi energy cross between Γ and A but are gapped beyond A since they possess the same spinor irrep beyond that *k* point. Although these bands are significantly below the Fermi level, they contribute to the $\mathbb{Z}_2$ characterization of this material and they provide insight into the interlayer electronic behavior.

To identify the origin of this crossing, a series of calculations was performed to track the evolution of the band structure and the relaxed physical structure as summarized in Fig. 3. From here on, when referring to electronic structure calculations unless indicated otherwise, this includes a structural relaxation, a self-consistent calculation, followed by band structure and DOS calculations in which the Fermi level for the band structure is taken from the DOS calculation given the more accurate sampling of *k* points (for more detailed
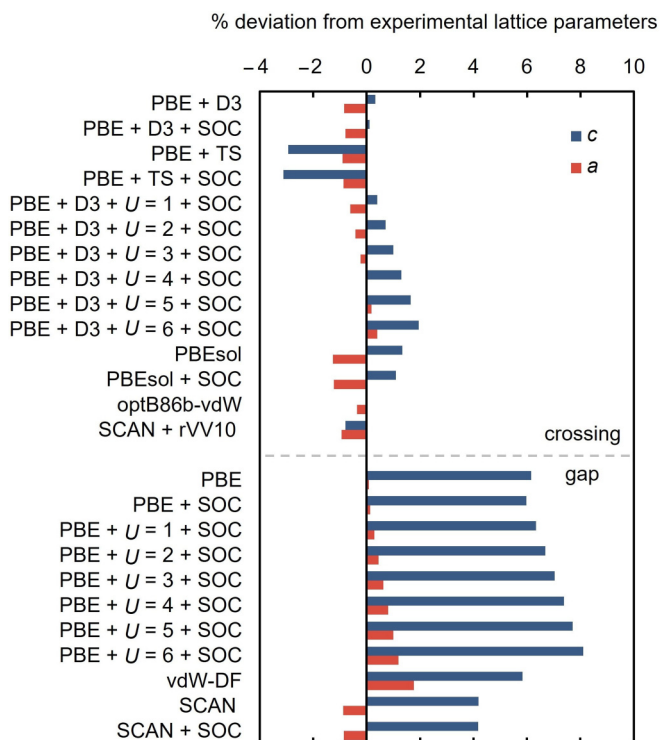
FIG. 3. Comparison of computationally relaxed to experimental lattice parameters. Low deviation from experimental values (specifically the *c* axis) coincides with the presence of a symmetry-allowed band crossing along Γ-*A*. The nonlocal van der Waals density functional optB86b-vdW yields a relaxed structure most similar to the experimental structure.

discussion see methods section). Each step in this procedure includes all listed parameters.

The first step in understanding this band crossing is finding what conditions give rise to the crossing. While the PBE+SOC+D3 band structure features the crossing, the PBE and PBE+SOC band structures show gapped bands. This result indicates that the D3 van der Waals correction is responsible for the crossing. The effect from the D3 correction can be either electronic (i.e., from the calculation) or structural (i.e., from the relaxation which produces a slightly different structure). To figure out why the D3 correction creates this band crossing, we performed unrelaxed calculations on the experimental structure. Since the unrelaxed PBE, PBE+SOC, and PBE+SOC+D3 calculations all show the band crossing, we conclude that the effect from the D3 correction in the relaxed calculation is structural. In other words, the relaxation with D3 produces a structure that closely resembles the experimental structure which already features a band crossing along Γ-*A*.

C. Comparison of band dispersion corrections

It is well documented that DFT methods over-delocalize electrons leading to overly dispersed bands [38,39]. These errors are potentially most pronounced for band dispersions along the out-of-plane direction within quasi-two-dimensional materials like the AV$_3$Sb$_5$ kagome compounds. Within the Brillouin zone (Fig. 2), this direction is represented

by the Γ-*A*, *K-H*, and *M-L* paths, meaning that these paths are more likely affected by overdispersion. Since the crossing of interest is along Γ-*A*, any correction of the band dispersion (i.e., decreasing the bandwidth) could open a gap between the two bands.

To probe the conditions under which a gap might open between the bands and thereby assess the robustness of this crossing, we compare a variety of commonly applied DFT approaches that address anisotropic nonlocal exchange and correlation at various levels. Again, all parameters or techniques were benchmarked against experimental or unrelaxed results to parse the electronic and structural contributions. Within electronic structure theory, there are a variety of methods to deal with localized electrons, including (1) adding a Hubbard U correction to specific orbitals, (2) adding an energetic correction term, (3) switching to a different exchange-correlation functional, and (4) turning to more advanced methods that more accurately treat band dispersions. While the following results do not constitute an exhaustive selection of all methods impacting band dispersion, a representative set of calculations within all of these categories was performed to provide generalized results as summarized in Fig. 3. Methods were selected based on their computational accessibility and the specificity of the correction to the interlayer band dispersion. Under these different computational conditions, other regions of the band structure also undergo minor changes. For example, the inclusion of SOC will open gaps between bands across the Brillouin zone. However, the most significant changes to the electronic structure within this survey of techniques occur along the Γ-*A* path. Additionally, for calculations that include SOC, the symmetry of the Brillouin zone paths outside of Γ-*A* dictates that bands will not cross, highlighting the importance of this particular interlayer direction in determining the necessary gap for $\mathbb{Z}_2$ calculations.

Hubbard U corrections are commonly used because they provide a targeted method for dealing with electron over-delocalization usually in d and f orbitals in a tunable and computationally inexpensive way [40–43]. In the context of CsV$_3$Sb$_5$, primarily Sb p orbitals contribute to the near E_F bands at the Brillouin zone center. While p orbitals typically do not suffer from the same over-delocalization issues in DFT, adding a variable U to these orbitals is a valuable exercise for tracking the behavior of the crossing as a function of the bandwidths of the involved bands. As the value of the U is increased, the deviations along the a and c axes become progressively more positive signifying an expansion of the unit cell during relaxation. In the presence of the D3 van der Waals correction, calculations with a Hubbard U from 1 eV to 6 eV exhibit a crossing. Without the D3 correction, these calculations show fully gapped bands with high lattice parameter deviations along the c axis.

Since CsV$_3$Sb$_5$ is considered a quasi-two-dimensional material given the separation of the kagome layers, van der Waals corrections beyond the D3 term could provide more accurate band dispersions corresponding to localized electrons along the k_z direction. These van der Waals terms are total energy corrections that are added to the calculated Kohn-Sham DFT energy and, therefore, do not impact the fundamental electronic structure. The computational efficiency of adding these corrections and the relative success in matching experimental

lattice parameters make these terms a popular method for addressing van der Waals systems [44,45]. However, moving to less empirical van der Waals corrections like the Tkatchenko-Sheffler (TS) correction [46] does not yield an improvement in the relaxed lattice parameters. In fact, the *c*-axis lattice parameter is significantly shorter compared to the experimental value.

Changing the exchange-correlation functional can be a more rigorous method for incorporating dispersion changes within the electronic structure calculation. The broadly applicable and widely used PBE functional is one example of a GGA functional that incorporates the local electron density and the gradient of the density. PBE can be improved for solid-state systems by modifying the exchange and correlation gradient expansion terms resulting in the PBEsol functional [47]. For CsV_3Sb_5, PBEsol yielded a relaxed structure with lattice parameters within 2% deviation from the experimental values without the addition of any explicit van der Waals correction. Dispersion interactions can be approximated within the functional by using a nonlocal van der Waals density functional that includes a nonlocal correlation term [48–51]. For this system, the optB86b-vdW and the SCAN+rVV10 functionals show similar values to the experimental lattice parameters, while the original nonlocal van der Waals density functional (vdW-DF) shows significant deviation. Finally, using a meta-GGA functional that additionally takes into account the kinetic energy density has been shown to systematically improve results without a significant increase in computational cost [52,53]. The most popular implementation of a meta-GGA functional, SCAN (strongly constrained and appropriately normed), produces a relaxed structure with relatively high deviation from experimental lattice parameters and a band structure with gapped Sb bands.

All of these corrections and methods were additionally compared to unrelaxed calculations (see Appendix A for a full summary of relaxed and unrelaxed calculations) to deconvolute the structural and electronic contributions. Under almost all tested computational parameters, a crossing is observed between the Sb bands along Γ-*A*, pointing to the importance of the structural relaxation in controlling the presence of this crossing. However, both SCAN and the nonlocal van der Waals functional SCAN+rVV10 yield a gap between the the Sb bands for the unrelaxed structure as shown in Fig. 4. These calculations represent the only levels of theory within standard DFT where this gap is observed for the experimental structure.

Another class of functionals that can provide more accurate electronic structures combine Kohn-Sham and Hartree-Fock theories. These "hybrid" functionals improve upon standard Kohn-Sham functionals by calculating a portion of exchange using Hartree-Fock methods [54–57]. Hybrid functionals can either be unscreened where Hartree-Fock exchange is calculated at full range or screened where only short-range exchange is a linear combination of Hartree-Fock and Kohn-Sham exchange and both correlation and long-range exchange is treated at the Kohn-Sham level. The popular Heyd-Scuseria-Ernzerhof (HSE) hybrid functional is an example of a screened hybrid functional in which one-fourth of the short-range exchange comes from Hartree-Fock and the remaining three-fourths comes from PBE exchange, while all long-range exchange and all correlation come from PBE. A modification
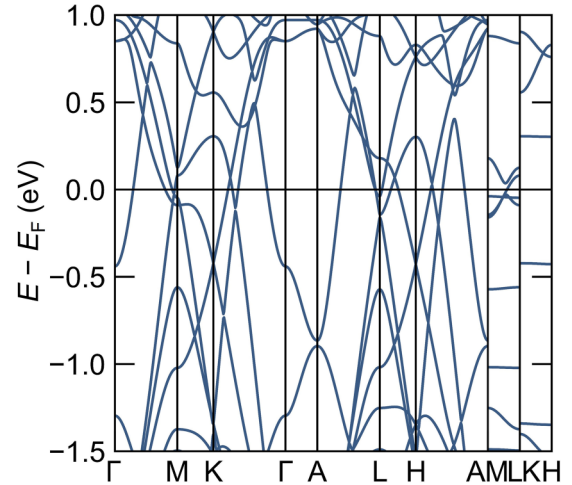

FIG. 4. Band structure calculated using the meta-GGA SCAN functional for the unrelaxed experimental structure.

of the HSE functional, HSEsol, replaces the contributions from PBE with PBEsol [58]. The distinction between short and long range is specified through a screening parameter [59,60].

Since unrelaxed HSE (HSE06) and HSEsol give band structures with negligible differences, we focus on the HSE results. While the band dispersions do not change significantly from non-hybrid DFT calculations, many of the bands experience a downward shift in energy as shown in Fig. 5. As a result of these shifts, the two Sb bands along Γ-*A* are gapped to an even greater extent than in the SCAN calculation.

Moving outside of the framework of DFT can also provide a more accurate picture of the electronic structure. For example, using the *GW* approximation for the electronic self-energy can appropriately narrow bands by more accurately capturing electron exchange and correlation, however, at higher computational cost. The *GW* approximation relies on a quasiparticle picture of the system in which electrons are "dressed" with positively charged polarization clouds due to the Coulomb repulsion of other electrons. These quasiparticles, which can be described using single-particle Green's functions (*G*), interact weakly via a dynamically screened Coulomb potential (*W*). Typically, *GW* calculations provide good estimates of the band energies and dispersions when comparing electronic structures from theory and experiment. Since *GW* calculations capture correlations stemming from dynamical and nonlocal density fluctuations, these calculations are well suited for systems in which van der Waals forces play a role. For CsV_3Sb_5, these types of interactions likely dominate the interlayer electronic behavior, meaning that the *GW* approximation provides inherent advantages over static mean field methods like Kohn-Sham DFT.

GW calculations were performed on the experimental structure without SOC and compared to a range of DFT results using PBE, SCAN, HSE, and nonlocal van der Waals density functionals (vdW-DF, optB86b, SCAN+rVV10) [48–52]. Single-shot G_0W_0 and partially self-consistent eigenvalue GW_0 yield similar band behavior as shown in Fig. 5,
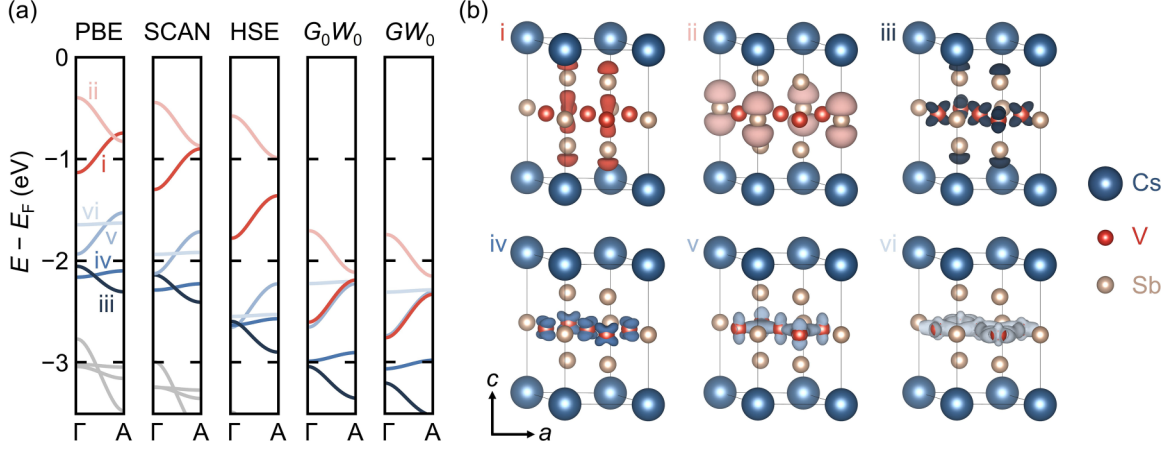
FIG. 5. DFT and *GW* interlayer electronic structure behavior. (a) Comparison of PBE, SCAN, HSE, single-shot G_0W_0, and partially self-consistent eigenvalue GW_0 band structures along Γ-A shows consistent band dispersions yet significant energetic shifts with the opening of the crossing between Sb bands in SCAN, HSE, and *GW*. (b) Band-decomposed charge densities corresponding to bands in (a) ordered by degree of interlayer character. (i) and (ii) show the out-of-kagome-plane and in-kagome-plane Sb p_z charge density, respectively, while (iii), (iv), (v), and (vi) show V *d* charge density with decreasing interlayer intensity.

indicating that single-shot calculations will give a relatively consistent picture of the band structure. Across the selected DFT and *GW* calculations, the dispersions of the bands highlighted in Fig. 5 have a maximum change of 72 meV (corresponding to the difference in dispersion of band iii between the GW_0 and vdW-DF calculations). For the Sb bands, i and ii, the dispersions across these methods differ by a maximum of 39 meV and 28 meV, respectively.

While the dispersions of the revelant bands remain relatively consistent when moving to *GW* calculations, all bands experience significant energy shifts and reordering especially below the Fermi level as indicated in Fig. 5. In particular, the two Sb bands shift downward by more than 1 eV, combining these bands with lower-lying less-dispersive V bands that experience less than 1 eV shifts downward. This shift induces a reordering of bands as some V bands now lie between the two Sb bands. Quantifying the quasiparticle energy shifts at Γ and A shows larger shifts of around 1.6 eV and 1.3 eV for p_z bands associated with Sb outside the kagome layer and within the kagome layer, respectively, and smaller shifts of 0.80 eV and 0.65 eV for V d_{z^2} and V d_{xy/x^2-y^2} bands, respectively. Orbital contributions are attributed based on band-decomposed charge densities depicted in Fig. 5(b) and published electronic structures with orbital projections [28,29]. The relative energy shifts of bands with varying degrees of interlayer character ultimately results in bands that are fully gapped between Γ and A.

IV. DISCUSSION

Within standard DFT, various band dispersion correction terms and methods lead to a similar conclusion: when the structure matches or is comparable to the experimental structure, the associated band structure will feature a symmetry-allowed crossing along Γ-A. This conclusion is evident in relaxed calculations; when there is a small deviation between the relaxed and experimental lattice parameters, a crossing is observed. Unrelaxed calculations reinforce this result by showing a crossing that is robust to a variety of

electronic corrections and terms. Additionally, the dispersions of the Sb bands that introduce the crossing are maintained across a variety of functionals and in *GW* calculations. However, in moving to higher levels of theory like meta-GGA functionals, hybrid functionals, or *GW* calculations, these Sb bands are gapped for the unrelaxed structure. This gap arises from the relevant bands shifting in energy and not from changes in the band dispersions. In *GW* calculations, these shifts are more pronounced for bands with higher degrees of interlayer orbital character. For example, the purely intralayer V d_{xy/x^2-y^2} bands experience the smallest shift in quasiparticle versus Kohn-Sham energies, whereas the out-of-plane Sb p_z band experiences the largest shift. Since the in-plane Sb band does not shift as much as the out-of-plane Sb, a gap is expected to open between these bands (note the separation between bands i and ii in Fig. 5).

Based on DFT calculations, the presence of this symmetry-allowed crossing and its robustness with a variety of band dispersion corrections suggests a reevaluation of the electronic structure of CsV_3Sb_5 specifically along the k_z direction. *GW* calculations provide further insights into the interlayer electronic structure, revealing a gap due to significant energetic shifts of bands below the Fermi level. Additionally, these results show interlayer interactions mediated through the V and out-of-plane Sb atoms indicated by the almost degenerate i and v bands shown in Fig. 5. The hybridization of these states suggests more interlayer phenomena at play than indicated in previous electronic structures.

Given the two-dimensionality of this kagome system, it is particularly important to study the interlayer electronic behavior as has been demonstrated computationally and experimentally with effects due to pressure and chemical doping and charge-density wave ordering [30,33,34,61]. All of these phenomena show dramatic changes along the *c* or k_z axes pointing to the critical role of understanding interlayer interactions. Rigorous electronic structure calculations capturing the k_z dispersion are further necessary since experimental verification of theses bands via ARPES remains challenging. The highly two-dimensional single crystals make it difficult

to obtain a clean surface required for the technique along the relevant axis.

Additionally, the Γ-A crossing (or lack thereof) has greater implications in the topological characterization of this system via $\mathbb{Z}_2$-invariant calculations. A crossing implies the absence of a continuous gap necessary for Fu-Kane $\mathbb{Z}_2$ calculations across a band manifold. In the case of CsV_3Sb_5, two near-Fermi-level gaps were included in the original $\mathbb{Z}_2$ analysis with both gaps yielding nontrivial $\mathbb{Z}_2$ invariants. However, based on the irrep analysis of this band structure (PBE+SOC+D3), one of these gaps is not a continuous gap due to the band crossing along Γ-A. While this symmetry analysis invalidates this lower gap, the upper gap (which can be seen above the crossing in Fig. 2) remains continuous throughout the entire Brillouin zone and maintains a nontrivial $\mathbb{Z}_2$ invariant. Since the Fu-Kane method involves taking the product of parity eigenvalues, the ordering of bands below the continuous gap does not affect the overall result meaning that the $\mathbb{Z}_2$ calculation for this particular gap is unchanged from previous reports even with the band reordering along Γ-A seen in the *GW* results [12]. Ultimately, the presence or absence of this symmetry-allowed crossing does not change the nontrivial $\mathbb{Z}_2$ classification even though it potentially reduces the number of continuous gaps. However, in other systems that do not have additional continuous gaps, subtle crossings that are not identified until irreps are considered could have more severe consequences on topological-invariant calculations.

This study motivates revisiting the protocol for defining $\mathbb{Z}_2$ invariants in metallic systems. Since the Fu-Kane method was originally intended for insulators, the presence of a gap and, subsequently, a separable band manifold is guaranteed by the system [7]. However, when moving to metals, this condition of separable bands becomes a prerequisite step before continuing with the calculation. From this study of CsV_3Sb_5, we find that visual identification of a near-Fermi-level gap that extends throughout the entire Brillouin zone is not always sufficient fulfillment of this prerequisite. Our results highlight the importance of confirming a gap via irreps prior to performing $\mathbb{Z}_2$ analysis in metals.

Finally, broader lessons regarding the interpretation of band structures can be learned from this study of CsV_3Sb_5. For example, recognizing that most band structure outputs do not include band symmetries and can, therefore, misidentify "continuous" bands advocates the integration of irrep analysis when depicting and understanding band structures. This lack of proper band tracking is reinforced if other computational parameters like k-point density along the Brillouin zone path are not high enough to resolve small features. These issues are crucial when attempting to calculate topological invariants based on bulk band structures but are also widely applicable to any system in which an accurate picture of the electronic structure is necessary.

V. CONCLUSION

Using first-principles calculations, we have identified variable band behavior along the interlayer direction in CsV_3Sb_5. Given the two-dimensional nature of this system, capturing the electronic structure along the c or k_z direction is experimentally and computationally difficult. In this study, we

TABLE I. Summary of unrelaxed and relaxed calculations showing which levels of theory yield crossing bands ($\times$) or gapped bands ($\bullet$) along Γ-A.

Computational parameters	Experimental structure	Relaxed structure
PBE	$\times$	$\bullet$
PBE + SOC	$\times$	$\bullet$
PBE + D3	$\times$	$\times$
PBE + D3 + SOC	$\times$	$\times$
PBE + TS	$\times$	$\times$
PBE + TS + SOC	$\times$	$\times$
PBE + $U = 1$ eV + SOC	$\times$	$\bullet$
PBE + $U = 2$ eV + SOC	$\times$	$\bullet$
PBE + $U = 3$ eV + SOC	$\times$	$\bullet$
PBE + $U = 4$ eV + SOC	$\times$	$\bullet$
PBE + $U = 5$ eV + SOC	$\times$	$\bullet$
PBE + $U = 6$ eV + SOC	$\times$	$\bullet$
PBE + D3 + $U = 1$ eV + SOC	$\times$	$\times$
PBE + D3 + $U = 2$ eV + SOC	$\times$	$\times$
PBE + D3 + $U = 3$ eV + SOC	$\times$	$\times$
PBE + D3 + $U = 4$ eV + SOC	$\times$	$\times$
PBE + D3 + $U = 5$ eV + SOC	$\times$	$\times$
PBE + D3 + $U = 6$ eV + SOC	$\times$	$\times$
PBEsol	$\times$	$\times$
PBEsol + SOC	$\times$	$\times$
SCAN	$\bullet$	$\bullet$
SCAN + SOC	$\times$	$\bullet$
SCAN + rVV10	$\bullet$	$\times$
optB86b-vdW	$\times$	$\times$
vdW-DF	$\times$	$\bullet$
HSE06	$\bullet$	
HSEsol	$\bullet$	
G_0W_0	$\bullet$	
ev GW_0	$\bullet$	

survey a variety of computational methods to address nonlocal exchange and correlation at different scales. Density functional theory calculations show a symmetry-allowed crossing along the k_z dispersion that arises due to the structural effect of dispersion corrections and methods employed during relaxation to more closely match experimental lattice parameters. This crossing is revealed upon irrep analysis of the bands. Yet, in turning toward higher levels of computational theory, this crossing is absent due to relative energy shifts of bands. By including dynamical nonlocal correlation via the *GW* approximation, we observe the near degeneracy of a V band and an out-of-kagome-plane Sb band. This interlayer electronic structure points to increased interactions occurring out of the kagome plane and serves as a baseline band structure for further studies of inter-kagome-layer phenomena.

APPENDIX A: SUMMARY OF CALCULATIONS

Our summary of calculations is given in Table I.

APPENDIX B: PLOTTING ELECTRONIC STRUCTURES

Since typical band structure data include the k points and energies of each band, portions of this data need to be rearranged to reflect the true band identity confirmed by irreps. For example, if two bands cross between k point 1 and k point 2, the output may incorrectly identify all lower energies as a continuous band and similarly all higher energies as another continuous band. In other words, the lower energy band before the crossing will be spuriously connected to the lower energy band after the crossing. However, looking at the irreps at k point 1 and k point 2 will indicate there is a crossing because the irreps switch between the two k points. This weakness in the output can be corrected by identifying the point at which the crossing occurs and reconnecting the bands to match the irrep results. This practice can be seen in Fig. 2 where the bands between Γ and A have been reconnected and colored to match the irreps.

The GW band structures in Fig. 5 were constructed based on the unrelaxed PBE band structure. Once the bands were reconnected based on irreps, each band was rescaled and repositioned according to the renormalization computed in the G_0W_0 and GW_0 calculations at Γ and at A. As such, bands from the GW output may suffer from the same misidentification across crossings; however, since only the energies and not the orbitals are updated in the employed partially self-consistent scheme, the GW energies can be properly matched based on the ordering of bands from the original PBE band structure.

[1] J. Xiao and B. Yan, First-principles calculations for topological quantum materials, Nat. Rev. Phys. **3**, 283 (2021).

[2] B. Bradlyn, L. Elcoro, J. Cano, M. G. Vergniory, Z. Wang, C. Felser, M. I. Aroyo, and B. A. Bernevig, Topological quantum chemistry, Nature (London) **547**, 298 (2017).

[3] A. Bansil, H. Lin, and T. Das, Colloquium: Topological band theory, Rev. Mod. Phys. **88**, 021004 (2016).

[4] C. L. Kane and E. J. Mele, Z_2 topological order and the quantum spin Hall effect, Phys. Rev. Lett. **95**, 146802 (2005).

[5] L. Fu, C. L. Kane, and E. J. Mele, Topological insulators in three dimensions, Phys. Rev. Lett. **98**, 106803 (2007).

[6] J. E. Moore and L. Balents, Topological invariants of time-reversal-invariant band structures, Phys. Rev. B **75**, 121306(R) (2007).

[7] L. Fu and C. L. Kane, Topological insulators with inversion symmetry, Phys. Rev. B **76**, 045302 (2007).

[8] L. M. Schoop, L. S. Xie, R. Chen, Q. D. Gibson, S. H. Lapidus, I. Kimchi, M. Hirschberger, N. Haldolaarachchige, M. N. Ali, C. A. Belvin, T. Liang, J. B. Neaton, N. P. Ong, A. Vishwanath, and R. J. Cava, Dirac metal to topological metal transition at a structural phase change in Au$_2$Pb and prediction of Z_2 topology for the superconductor, Phys. Rev. B **91**, 214517 (2015).

[9] J. Qian, Z. Shen, X. Wei, and W. Li, Z_2 nontrivial topology of rare-earth binary oxide superconductor LaO, Phys. Rev. B **105**, L020508 (2022).

[10] J. Nayak, S.-C. Wu, N. Kumar, C. Shekhar, S. Singh, J. Fink, E. E. D. Rienks, G. H. Fecher, S. S. P. Parkin, B. Yan, and C. Felser, Multiple Dirac cones at the surface of the topological metal LaBi, Nat. Commun. **8**, 13942 (2017).

[11] B. R. Ortiz, P. M. Sarte, E. M. Kenney, M. J. Graf, S. M. L. Teicher, R. Seshadri, and S. D. Wilson, Superconductivity in the Z_2 kagome metal KV$_3$Sb$_5$, Phys. Rev. Mater. **5**, 034801 (2021).

[12] B. R. Ortiz, S. M. L. Teicher, Y. Hu, J. L. Zuo, P. M. Sarte, E. C. Schueller, A. M. M. Abeykoon, M. J. Krogstad, S. Rosenkranz, R. Osborn, R. Seshadri, L. Balents, J. He, and S. D. Wilson, CsV$_3$Sb$_5$: A Z_2 topological kagome metal with a superconducting ground state, Phys. Rev. Lett. **125**, 247002 (2020).

[13] S. Yan, D. A. Huse, and S. R. White, Spin-liquid ground state of the $S = 1/2$ kagome Heisenberg antiferromagnet, Science **332**, 1173 (2011).

[14] W.-H. Ko, P. A. Lee, and X.-G. Wen, Doped kagome system as exotic superconductor, Phys. Rev. B **79**, 214502 (2009).

[15] H.-M. Guo and M. Franz, Topological insulator on the kagome lattice, Phys. Rev. B **80**, 113102 (2009).

[16] J. P. Perdew, K. Burke, and M. Ernzerhof, Generalized gradient approximation made simple, Phys. Rev. Lett. **77**, 3865 (1996).

[17] S. Grimme, J. Antony, S. Ehrlich, and H. Krieg, A consistent and accurate *ab initio* parametrization of density functional dispersion correction (DFT-D) for the 94 elements H–Pu, J. Chem. Phys. **132**, 154104 (2010).

[18] S. Grimme, S. Ehrlich, and L. Goerigk, Effect of the damping function in dispersion corrected density functional theory, J. Comput. Chem. **32**, 1456 (2011).

[19] B. R. Ortiz, L. C. Gomes, J. R. Morey, M. Winiarski, M. Bordelon, J. S. Mangum, I. W. H. Oswald, J. A. Rodriguez-Rivera, J. R. Neilson, S. D. Wilson, E. Ertekin, T. M. McQueen, and E. S. Toberer, New kagome prototype materials: Discovery of KV$_3$Sb$_5$, RbV$_3$Sb$_5$, and CsV$_3$Sb$_5$, Phys. Rev. Mater. **3**, 094407 (2019).

[20] M. Methfessel and A. T. Paxton, High-precision sampling for Brillouin-zone integration in metals, Phys. Rev. B **40**, 3616 (1989).

[21] P. E. Blöchl, O. Jepsen, and O. K. Andersen, Improved tetrahedron method for Brillouin-zone integrations, Phys. Rev. B **49**, 16223 (1994).

[22] S. Curtarolo, W. Setyawan, G. L. Hart, M. Jahnatek, R. V. Chepulskii, R. H. Taylor, S. Wang, J. Xue, K. Yang, O. Levy, M. J. Mehl, H. T. Stokes, D. O. Demchenko, and D. Morgan,

AFLOW: An automatic framework for high-throughput materials discovery, Comput. Mater. Sci. **58**, 218 (2012).

[23] A. M. Ganose, A. J. Jackson, and D. O. Scanlon, sumo: Command-line tools for plotting and analysis of periodic *ab initio* calculations, J. Open Source Software **3**, 717 (2018).

[24] J. Gao, Q. Wu, C. Persson, and Z. Wang, Irvsp: To obtain irreducible representations of electronic states in the VASP, Comput. Phys. Commun. **261**, 107760 (2021).

[25] Z. Hao, Y. Cai, Y. Liu, Y. Wang, X. Sui, X.-M. Ma, Z. Shen, Z. Jiang, Y. Yang, W. Liu, Q. Jiang, Z. Liu, M. Ye, D. Shen, Y. Liu, S. Cui, J. Chen, L. Wang, C. Liu, J. Lin *et al.*, Dirac nodal lines and nodal loops in the topological kagome superconductor CsV_3Sb_5, Phys. Rev. B **106**, L081101 (2022).

[26] Y. Hu, S. M. Teicher, B. R. Ortiz, Y. Luo, S. Peng, L. Huai, J. Ma, N. C. Plumb, S. D. Wilson, J. He, and M. Shi, Topological surface states and flat bands in the kagome superconductor CsV_3Sb_5, Sci. Bull. **67**, 495 (2022).

[27] M. Kang, S. Fang, J.-K. Kim, B. R. Ortiz, S. H. Ryu, J. Kim, J. Yoo, G. Sangiovanni, D. Di Sante, B.-G. Park, C. Jozwiak, A. Bostwick, E. Rotenberg, E. Kaxiras, S. D. Wilson, J.-H. Park, and R. Comin, Twofold van Hove singularity and origin of charge order in topological kagome superconductor CsV_3Sb_5, Nat. Phys. **18**, 301 (2022).

[28] A. Tsirlin, P. Fertey, B. R. Ortiz, B. Klis, V. Merkl, M. Dressel, S. Wilson, and E. Uykur, Role of Sb in the superconducting kagome metal CsV_3Sb_5 revealed by its anisotropic compression, SciPost Phys. **12**, 049 (2022).

[29] C. Li, X. Wu, H. Liu, C. Polley, Q. Guo, Y. Wang, X. Han, M. Dendzik, M. H. Berntsen, B. Thiagarajan, Y. Shi, A. P. Schnyder, and O. Tjernberg, Coexistence of two intertwined charge density waves in a kagome system, Phys. Rev. Res. **4**, 033072 (2022).

[30] Y. M. Oey, B. R. Ortiz, F. Kaboudvand, J. Frassineti, E. Garcia, R. Cong, S. Sanna, V. F. Mitrović, R. Seshadri, and S. D. Wilson, Fermi level tuning and double-dome superconductivity in the kagome metal $CsV_3Sb_{5-x}Sn_x$, Phys. Rev. Mater. **6**, L041801 (2022).

[31] X. Huang, C. Guo, C. Putzke, M. Gutierrez-Amigo, Y. Sun, M. G. Vergniory, I. Errea, D. Chen, C. Felser, and P. J. W. Moll, Three-dimensional Fermi surfaces from charge order in layered CsV_3Sb_5, Phys. Rev. B **106**, 064510 (2022).

[32] E. Uykur, B. R. Ortiz, O. Iakutkina, M. Wenzel, S. D. Wilson, M. Dressel, and A. A. Tsirlin, Low-energy optical properties of the nonmagnetic kagome metal CsV_3Sb_5, Phys. Rev. B **104**, 045130 (2021).

[33] K. Y. Chen, N. N. Wang, Q. W. Yin, Y. H. Gu, K. Jiang, Z. J. Tu, C. S. Gong, Y. Uwatoko, J. P. Sun, H. C. Lei, J. P. Hu, and J.-G. Cheng, Double superconducting dome and triple enhancement of T_c in the kagome superconductor CsV_3Sb_5 under high pressure, Phys. Rev. Lett. **126**, 247001 (2021).

[34] F. Yu, X. Zhu, X. Wen, Z. Gui, Z. Li, Y. Han, T. Wu, Z. Wang, Z. Xiang, Z. Qiao, J. Ying, and X. Chen, Pressure-induced dimensional crossover in a kagome superconductor, Phys. Rev. Lett. **128**, 077001 (2022).

[35] M. S. Dresselhaus, G. Dresselhaus, and A. Jorio, *Group Theory: Application to the Physics of Condensed Matter* (Springer, Berlin, 2008), pp. 305–336.

[36] Y. X. Zhao and A. P. Schnyder, Nonsymmorphic symmetry-required band crossings in topological semimetals, Phys. Rev. B **94**, 195109 (2016).

[37] M. M. Hirschmann, A. Leonhardt, B. Kilic, D. H. Fabini, and A. P. Schnyder, Symmetry-enforced band crossings in tetragonal materials: Dirac and Weyl degeneracies on points, lines, and planes, Phys. Rev. Mater. **5**, 054202 (2021).

[38] D. S. Sholl and J. A. Steckel, *Density Functional Theory: A Practical Introduction* (Wiley, Hoboken, NJ, 2009), pp. 209–233.

[39] R. R. Martin, *Electronic Structure: Best Theory and Practical Methods* (Cambridge University Press, Cambridge, UK, 2004), pp. 152–171.

[40] V. I. Anisimov, J. Zaanen, and O. K. Andersen, Band theory and Mott insulators: Hubbard *U* instead of Stoner *I*, Phys. Rev. B **44**, 943 (1991).

[41] M. Cococcioni and S. de Gironcoli, Linear response approach to the calculation of the effective interaction parameters in the LDA + U method, Phys. Rev. B **71**, 035105 (2005).

[42] H. J. Kulik, Perspective: Treating electron over-delocalization with the DFT+U method, J. Chem. Phys. **142**, 240901 (2015).

[43] S. L. Dudarev, G. A. Botton, S. Y. Savrasov, C. J. Humphreys, and A. P. Sutton, Electron-energy-loss spectra and the structural stability of nickel oxide: An LSDA+U study, Phys. Rev. B **57**, 1505 (1998).

[44] W. Reckien, F. Janetzko, M. F. Peintinger, and T. Bredow, Implementation of empirical dispersion corrections to density functional theory for periodic systems, J. Comput. Chem. **33**, 2023 (2012).

[45] S. Grimme, A. Hansen, J. G. Brandenburg, and C. Bannwarth, Dispersion-corrected mean-field electronic structure methods, Chem. Rev. **116**, 5105 (2016).

[46] A. Tkatchenko and M. Scheffler, Accurate molecular van der Waals interactions from ground-state electron density and free-atom reference data, Phys. Rev. Lett. **102**, 073005 (2009).

[47] J. P. Perdew, A. Ruzsinszky, G. I. Csonka, O. A. Vydrov, G. E. Scuseria, L. A. Constantin, X. Zhou, and K. Burke, Restoring the density-gradient expansion for exchange in solids and surfaces, Phys. Rev. Lett. **100**, 136406 (2008).

[48] G. Román-Pérez and J. M. Soler, Efficient implementation of a van der Waals density functional: Application to double-wall carbon nanotubes, Phys. Rev. Lett. **103**, 096102 (2009).

[49] M. Dion, H. Rydberg, E. Schröder, D. C. Langreth, and B. I. Lundqvist, Van der Waals density functional for general geometries, Phys. Rev. Lett. **92**, 246401 (2004).

[50] H. Peng, Z.-H. Yang, J. P. Perdew, and J. Sun, Versatile van der Waals density functional based on a meta-generalized gradient approximation, Phys. Rev. X **6**, 041005 (2016).

[51] J. Klimeš, D. R. Bowler, and A. Michaelides, Van der Waals density functionals applied to solids, Phys. Rev. B **83**, 195131 (2011).

[52] J. Sun, A. Ruzsinszky, and J. P. Perdew, Strongly constrained and appropriately normed semilocal density functional, Phys. Rev. Lett. **115**, 036402 (2015).

[53] J. Sun, R. C. Remsing, Y. Zhang, Z. Sun, A. Ruzsinszky, H. Peng, Z. Yang, A. Paul, U. Waghmare, X. Wu, M. L. Klein, and J. P. Perdew, Accurate first-principles structures and energies of diversely bonded systems from an efficient density functional, Nat. Chem. **8**, 831 (2016).

[54] B. G. Janesko, T. M. Henderson, and G. E. Scuseria, Screened hybrid density functionals for solid-state chemistry and physics, Phys. Chem. Chem. Phys. **11**, 443 (2009).

[55] T. M. Henderson, J. Paier, and G. E. Scuseria, Accurate treatment of solids with the HSE screened hybrid, Phys. Status Solidi B **248**, 767 (2011).

[56] J. Heyd and G. E. Scuseria, Efficient hybrid density functional calculations in solids: Assessment of the Heyd-Scuseria-Ernzerhof screened Coulomb hybrid functional, J. Chem. Phys. **121**, 1187 (2004).

[57] J. Heyd, J. E. Peralta, G. E. Scuseria, and R. L. Martin, Energy band gaps and lattice parameters evaluated with the Heyd-Scuseria-Ernzerhof screened hybrid functional, J. Chem. Phys. **123**, 174101 (2005).

[58] L. Schimka, J. Harl, and G. Kresse, Improved hybrid functional for solids: The HSEsol functional, J. Chem. Phys. **134**, 024116 (2011).

[59] J. Heyd, G. E. Scuseria, and M. Ernzerhof, Hybrid functionals based on a screened Coulomb potential, J. Chem. Phys. **118**, 8207 (2003).

[60] A. V. Krukau, O. A. Vydrov, A. F. Izmaylov, and G. E. Scuseria, Influence of the exchange screening parameter on the performance of screened hybrid functionals, J. Chem. Phys. **125**, 224106 (2006).

[61] L. Kautzsch, B. R. Ortiz, K. Mallayya, J. Plumb, G. Pokharel, J. P. C. Ruff, Z. Islam, E.-A. Kim, R. Seshadri, and S. D. Wilson, Structural evolution of the kagome superconductors AV$_3$Sb$_5$ (A = K, Rb, and Cs) through charge density wave order, Phys. Rev. Mater. **7**, 024806 (2023).